Transonic flows of dense gases over finite wings

P. Cinnella
Dipartimento di Ingegneria dell'Innovazione, Università del Salento, via Monteroni, 73100 Lecce, Italy

(Received 7 December 2007; accepted 4 March 2008; published online 30 April 2008)

Transonic inviscid flows of dense gases of the Bethe–Zel'dovich–Thompson (BZT) type over finite wings are numerically investigated. BZT gases are fluids of the retrograde type (i.e., that superheat when expanded), which exhibit a region of negative values of the fundamental derivative of gas dynamics Γ. As a consequence, they display, in the transonic and supersonic regime, nonclassical gas dynamic behaviors, such as rarefaction shock waves and mixed shock/fan waves. The peculiar properties of BZT fluids have received increased interest in recent years because of their possible application in energy-conversion cycles. The present research aims at providing insight about the transonic aerodynamics of BZT fluids past finite wings, roughly representative of isolated turbine blades with infinite tip leakage. This represents an important step toward the design of advanced turbine blades by using organic working fluids. An investigation of the flow patterns and aerodynamic performance for several choices of the upstream thermodynamic conditions is provided, and the advantages of using BZT working fluids instead of classical ones are discussed.
© *2008 American Institute of Physics*. [DOI: 10.1063/1.2907212]

I. INTRODUCTION

The existence of nonclassical waves in gas dynamics has been theoretically demonstrated for transonic and supersonic flows of complex substances, displaying in their vapor phase negative values of the fundamental derivative of gas dynamics,[1]

$$\Gamma := 1 + \frac{\rho}{a}\left(\frac{\partial a}{\partial \rho}\right)_s \tag{1}$$

(with ρ the fluid density, a the sound speed, and s the entropy), for thermodynamic conditions near the liquid/vapor critical point and close to the liquid/vapor saturation curve. Such substances are referred- to as Bethe–Zel'dovich–Thompson (BZT) fluids, from the names of the researchers who for the first time postulated their existence. Γ represents a measure of the rate of change of the local propagation speed of weak pressure disturbances. For instance, for a simple right-running wave,[1]

$$\left(\frac{\partial w}{\partial \rho}\right)_s = \frac{a\Gamma}{\rho}, \tag{2}$$

where $w=u+a$ is the wave propagation speed (u being the local fluid velocity). Equation (2) shows that compression waves steepen to form a compression shock if $\Gamma>0$, but are smoothed out if $\Gamma<0$. On the contrary, for $\Gamma<0$, only expansion shocks are physically admissible. If $\Gamma=0$, both compression and expansion waves propagate in time without distortion. The thermodynamic region where nonclassical phenomena occur is called the *inversion zone* and the $\Gamma=0$ curve is called the *transition line*.[2] Moreover, for $\Gamma<1$, the sound speed decreases upon isentropic compression, contrarily to what happens in conventional fluids such as air or steam. Mathematical proofs of the existence and well posedness of nonclassical solutions of the Euler equations can be found in Ref. 3.

According to state-of-the-art thermodynamic models, a region of negative Γ exists for molecularly complex fluids, i.e., fluids composed by molecules characterized by a large number of degrees of freedom, such as heavy hydrocarbons,[4] perfluorocarbons,[4–6] and siloxanes.[7] The possibility of observing nonclassical waves increases for substances possessing large specific heats and molecular weight. Precisely, it strongly depends on the ratio $c_{v_\infty}(T_c)/R$, $c_{v_\infty}(T_c)$ being the specific heat at constant volume in the dilute gas limit and at the critical temperature, and $R=\mathcal{R}/M$ the gas constant (with $\mathcal{R}$ the universal constant of gases and M the gas molecular weight). Recently, Colonna and Guardone[8] have proposed a molecular interpretation of nonclassical gas dynamic effects for van der Waals gases. Namely, they show that the decrease of the sound speed upon isentropic compression, typical of nonclassical flow fields, is due to the van der Waals attractive forces, and that this effect is stronger for complex molecules with a large number of active vibrational modes.

Experimental evidence of nonclassical waves has been documented for liquid/vapor systems.[9–11] For single-phase gases close to saturation conditions, the most impressive nonclassical phenomenon, i.e., the formation of a rarefaction shock wave, has been experimentally observed by Borisov *et al.*[12] and by Kutateladze *et al.*[13] However, the interpretation of such results has been challenged by several authors.[9,14,15] Presently, considerable efforts are being carried out at the University of Colorado Boulder and at the University of Delft (the Netherlands) for providing an irrefutable experimental proof of the existence of rarefaction shocks in single-phase vapors.[15,16]

In spite of the difficulty of providing reliable experimental results for nonclassical flow fields, the theoretical and numerical study of nonclassical gas dynamics is an active research field (see Refs. 17–19 for reviews). A wealth of literature reports analytical and numerical studies of unconventional gas dynamic effects. For instance, nozzles and

 © 2008 American Institute of Physics

Downloaded 23 May 2011 to 200.17.228.160. Redistribution subject to AIP license or copyright; see http://pof.aip.org/about/rights_and_permissions

simple two-dimensional geometries have been studied in Refs. 20–22. Two-dimensional flows past isolated airfoils and through turbine cascades exhibiting nonclassical effects have been numerically studied in Refs. 23–28. The interest of researchers is strongly motivated by potential applications of BZT fluids in technology, and specifically by the potential advantages of their use as working fluids in organic Rankine cycles (ORCs).[20,27,28] These are energy-conversion cycles that use low-boiling organic substances instead of steam as the working fluid. ORC turbines typically work in the transonic/low supersonic regime, and their major loss mechanism is related to the generation of shock waves and their interactions with blade boundary layers. Therefore, on the one hand a detailed study of turbomachinery flows of dense gases is necessary to correctly predict the system behavior; on the other hand, nonclassical dense gas phenomena could be exploited to improve efficiency: Namely, shock formation and subsequent losses could be ideally suppressed, if turbine expansion could happen entirely within or in the immediate neighborhood of the inversion zone. Previous works about BZT transonic flows past airfoils[23] and through turbine cascades[27,28] show that, properly operating the turbine in the very neighborhood of the $\Gamma=0$ curve, the flow field evolves almost entirely within the inversion zone and is shock-free: As a result, except for viscous drag, the flow remains almost isentropic through the entire cascade. Unfortunately, because of the limited extent of the inversion zone, a reduction in the temperature jump between the heater and condenser stages is generally required in order to completely operate the turbine within it. This leads to poor Carnot cycle efficiency and cycle power output. The development of real-world BZT ORCs relies on the possibility of finding a reasonable trade-off between high turbine efficiency and global cycle efficiency and power output.

Recently, Cinnella and Congedo[29,30] have investigated the influence of dense gas effects on the aerodynamic performance of inviscid and viscous transonic lifting flows past a NACA0012 airfoil for a wide range of free-stream thermodynamic conditions. The gas response was modeled by the van der Waals equation of state for polytropic gases or by the more realistic Martin–Hou (MAH) equation.[31] Detailed parametric investigations were undertaken, with specific interest in configurations providing the best trade-off between high lift and low drag. Figure 1(a) shows, for instance, a representation in the Amagat plane of the saturation curve, the inversion zone, and Γ isolines for the BZT perfluorocarbon PP10 modeled through the MAH model. Symbols represent operating conditions used for the study of Ref. 30. The corresponding lift coefficient and aerodynamic efficiency at fixed free-stream Mach number and angle of attack ($M_\infty=0.85$, $\alpha=1°$, respectively) are displayed in Figs. 1(b) and 1(c). For flows characterized by small free-stream values of Γ [represented by white squares in Fig. 1(a)], results presented in other studies are recovered, namely, the flow is subcritical and characterized by zero wave drag. However, the lift coefficient is relatively low, with respect to a system using a perfect gas as the working fluid: This is the counterpart, for an airfoil, of the aforementioned trade-off between high turbine efficiency and high cycle power output for

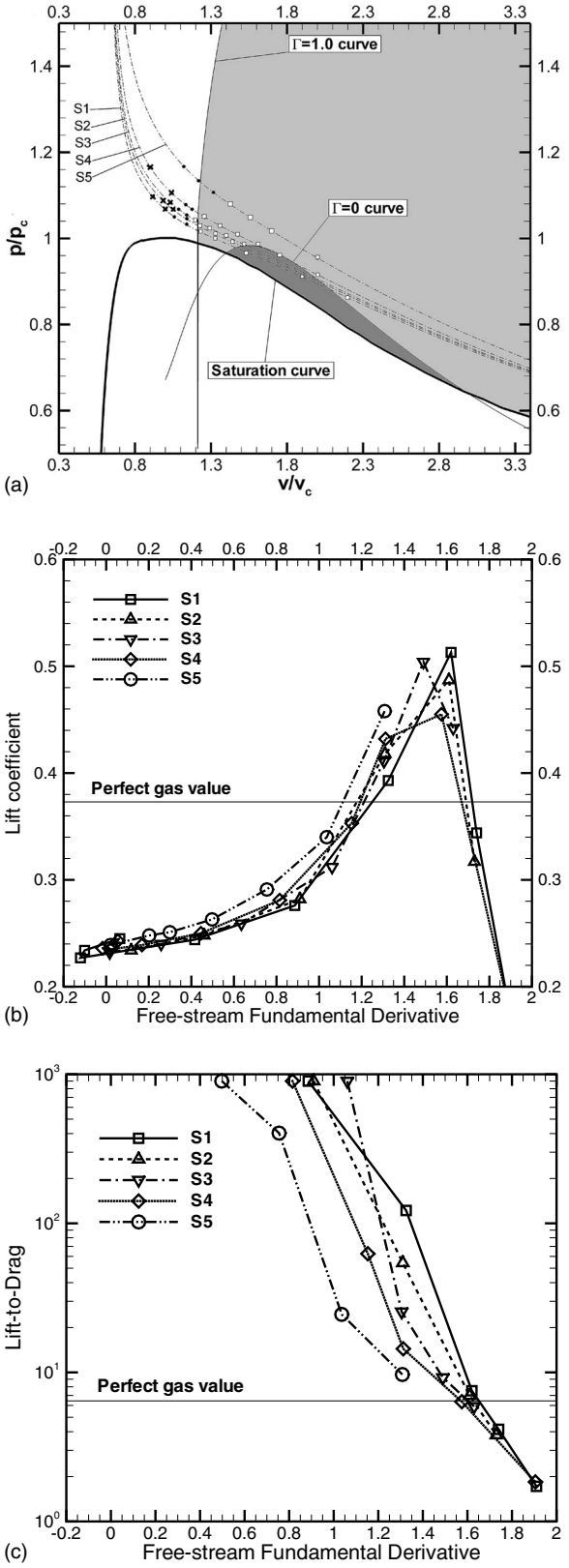

FIG. 1. Amagat plane for the BZT perfluorocarbon PP10 and location of the operation points used for the parametric study of Ref. 30 (a), and corresponding values of the lift coefficient (b) and lift-to-drag ratio (c) for flow at $M_\infty=0.85$, $\alpha=1°$ past a NACA0012 airfoil.

Downloaded 23 May 2011 to 200.17.228.160. Redistribution subject to AIP license or copyright; see http://pof.aip.org/about/rights_and_permissions

energy-conversion systems. By increasing the operating pressure and density, Γ becomes $O(1)$ [points represented by black circles in Fig. 1(a)], and a significant growth in both lift and drag is observed: The increase in lift is produced by the formation of an expansion shock, close to the leading edge, which strongly enhances the suction peak at the airfoil upper surface; the increase in drag is due to the occurrence of shock waves in the flow field. Nevertheless, losses introduced by such discontinuities are very low, due to the smallness of entropy changes across weak shocks in the vicinity of the transition line, and the lift-to-drag ratio remains one order of magnitude greater than in perfect gas flow. Finally, when Γ_∞ reaches higher values, far from the inversion zone [points represented by crosses in Fig. 1(a)], the flow becomes qualitatively similar to that of a classical gas, with even poorer performance and the benefits due to BZT effects progressively disappear. In summary, the results presented in Refs. 29 and 30 suggest that the choice of upstream conditions within or very close to the transition line is not only *not* mandatory in order to improve airfoil performance, as suggested in previous studies, but also not optimal. Specifically, optimal aerodynamic performance (i.e., the best trade-off between high lift and low drag) is obtained for free-stream thermodynamic conditions such that $\Gamma_\infty = O(1)$ and the second nonlinearity parameter, $\Lambda_\infty := \rho_\infty (\partial\Gamma/\partial\rho)_{s|\infty}$ (i.e., the rate of change of Γ in isentropic perturbations), is positive: These conditions are met at the high-pressure side of the inversion zone. Significant performance improvements can be also achieved for thermodynamic conditions, such that the flow evolves entirely outside the inversion zone, provided that the (positive) fundamental derivative at the wall remains sufficiently lower than one.[30] In practice, the above-mentioned results suggest the possibility of working partly outside the inversion zone without loosing the benefits of dense gas effects. Similarly, numerical computations of flows through two-dimensional (2D) turbine cascades show performance improvement for operating conditions (turbine inlet conditions) located at the upper side of the inversion zone, with inlet Γ values of the order of 1.

Results previously reported in the literature concern only 2D flows past airfoils and turbine blades. In practice, it is well known from classical aerodynamics that three-dimensional (3D) effects play a crucial role in the aerodynamic performance of lifting surfaces. Specifically, lifting wings of finite span exhibit additional drag induced by tip vortices, whose magnitude is inversely proportional to the wing aspect ratio (i.e., span-to-chord ratio) and directly proportional to the square of the lift coefficient. Similarly, in turbomachinery, additional losses due to leakage flow appear (in addition to losses related to 3D viscous effects due to end-wall boundary layers, secondary flows, etc.), which are inversely proportional to the blade aspect ratio and directly proportional to the square of the blade lift coefficient.[32] A detailed knowledge of the finite wing aerodynamics for dense gases is of paramount importance, namely, for the design of turbine blades working in the transonic regime, for which there is little analytic theory for guidance in the design process. This is particularly true for flows of BZT gases: For these flows, besides the simultaneous presence of elliptic and hyperbolic regions, the flow fields may also exhibit both positive and negative hyperbolic behaviors due to the change in sign of the fundamental derivative. In general, for dense gas flows no quantitative information is available in the literature about how design choices such as the blade aspect ratio, taper ratio, sweep angle, and twist influence the aerodynamic performance even if, at least qualitatively, trends may be expected to be similar to those observed for classical flows. Most of all, it is important to determine to what extent 3D effects influence the ranges of thermodynamic operating conditions—their location and their extent—where dense gas effects can be usefully exploited to increase the system efficiency.

In the past, calculations of 3D BZT gas flows were presented in Refs. 33 and 34 for a dense gas shock tube configuration and aimed at investigating the influence of diaphragm bursting on wave formation and propagation. To the author's best knowledge, no results for 3D dense gas flows over wings have been previously reported in the literature. Even if the final goal of the present research is the development of BZT turbines, a detailed study of transonic finite wing aerodynamics for flows of dense gases is first carried out in order to understand how 3D effects influence system losses for a simple configuration. This allows gaining insight of 3D BZT flows over lifting surfaces before tackling the study of much more complex turbine flows. The geometrical configurations adopted for the study, i.e., isolated finite wings, can be considered as roughly representative of isolated turbine blades with infinite tip leakage. The aerodynamic performance of dense gas flows is studied for simple rectangular wings of different aspect ratios as well as for the well-known ONERA M-6 swept wing, which is also used for validation purposes. Simulations are performed over a wide range of thermodynamic conditions and for several choices of the working fluid. For each configuration, the effects of the working fluid, of the operating thermodynamic conditions, and of the wing planform are investigated, and the results are compared to those obtained for a rectangular wing of infinite aspect ratio (2D case) using the same baseline airfoil.

II. GOVERNING EQUATIONS AND NUMERICAL METHOD

Since dense gas effects mainly influence inviscid flow behavior, the present analyses are restricted to the Euler equations for compressible single-phase flows, written in integral form for a control volume Ω with boundary $\partial\Omega$,

$$\frac{d}{dt}\int_\Omega w d\Omega + \oint_{\partial\Omega} \mathbf{f}\cdot\mathbf{n} dS = 0. \tag{3}$$

In Eq. (3), $w=(\rho,\rho\mathbf{v},\rho E)^T$ (with $\mathbf{v}$ the velocity vector, $E=e+|\mathbf{v}|^2/2$ the total energy per unit mass, and e the internal energy per unit mass) is the conservative variable vector, $\mathbf{n}$ is the unit outer normal to Ω, and $\mathbf{f}$ is the flux density, given by

Downloaded 23 May 2011 to 200.17.228.160. Redistribution subject to AIP license or copyright; see http://pof.aip.org/about/rights_and_permissions

$$\mathbf{f} = (\rho\mathbf{v}, \rho\mathbf{v}\mathbf{v} + p\bar{\bar{I}}, \rho\mathbf{v}H)^T,$$

with p the fluid pressure, $H=E+p/\rho$ the total enthalpy per unit mass, and $\bar{\bar{I}}$ the unit tensor.

Equation (3) is completed by a thermal equation of state,

$$p = p(\rho, T)$$

and a caloric equation of state,

$$e = e(\rho, T),$$

T being the absolute temperature. The latter is related to the first one through the compatibility relation,

$$e = e_r + \int_{T_r}^{T} c_{v_\infty} dT' - \int_{\rho_r}^{\rho} \left[T\left(\frac{\partial p}{\partial T}\right)_\rho - p \right] \frac{d\rho'}{\rho'^2}.$$

In the above, $c_{v_\infty}=c_{v_\infty}(T)$ is the low pressure, i.e., ideal gas, specific heat at constant volume, subscript r indicates a reference state, and T' and ρ' are auxiliary integration variables. The caloric equation of state is completely determined once a variation law for c_{v_∞} is specified.

In the present work, the MAH thermal equation of state is used,[31] which is considered to provide a realistic description of the gas behavior close to saturation and of the inversion zone size.[35,36] Such equation, involving five virial terms and satisfying ten thermodynamic constraints, ensures high accuracy with a minimum amount of experimental information. A power law of the form

$$c_{v_\infty} = c_{v_\infty}(T_c)\left(\frac{T}{T_c}\right)^n$$

is used to model variations of the low-density specific heat with temperature, where n is a material-dependent parameter.

In most of the following computations, the working fluid is the BZT gas *pf*-perhydrofluorene ($C_{13}F_{22}$, commercial name PP10). The material-dependent quantities required by the thermodynamic models include the boiling temperature, critical pressure and temperature, and the nondimensional critical low-density specific heat $[c_{v_\infty}(T_c)/R]$. The last parameter strongly affects the BZT behavior of gases: The larger it is, the larger the extent of the inversion zone.[6] The required data for PP10 have been taken from Ref. 5. Because of the difficulty of gathering reliable experimental data for critical point quantities, such values are likely to be affected by significant errors. A study of the sensitivity of the MAH thermodynamic model to input parameters has been performed in Ref. 6: The size of the inversion zone is found to be very sensitive to the critical temperature and to the boiling temperature at one atmosphere, whereas its sensitivity to other parameters (such as the critical pressure, the critical compressibility factor, and the critical point specific heat) is much less accentuated. Note, however, that if absolute values are likely to change, this does not significantly alter the predicted trends. For instance, results of Ref. 29, based on the very rough polytropic van der Waals gas model, are qualitatively similar, in terms of trends of variation of the aerodynamic coefficients with the operating thermodynamic conditions, to those obtained in Ref. 30 under the MAH model.

To investigate the influence of the material properties on the predicted results, in the present work some computations are performed also for the BZT fluid decamethylcyclopentasiloxane ($C_{10}H_{30}O_5Si_5$, commercial name D5) characterized by a nondimensional specific heat close to that of PP10, but lower critical temperature and pressure, and for a lighter, non-BZT fluid, namely, toluene (C_7H_8). For this fluid, the fundamental derivative is positive for all choices of the thermodynamic conditions in the vapor phase. Finally, the results are also reported for a diatomic perfect gas, representative of a generic conventional fluid and taken as a reference.

The governing equations are discretized using a cell-centered finite volume scheme of third-order accuracy, extended to the computation of flows with an arbitrary equation of state.[37] The scheme is constructed by correcting the dispersive error term of second-order-accurate Jameson's scheme.[38] The use of a scalar dissipation term simplifies the scheme implementation with highly complex equations of state and greatly reduces computational costs. The high accuracy of the scheme is preserved also on non-Cartesian grids due to the use of suitably weighted discretization formulas, which take into account mesh deformations, for the numerical fluxes: This ensures truly third-order accuracy on moderately deformed meshes and at least second-order accuracy on highly distorted meshes (see Ref. 39 for details). The governing equations are integrated in time by using a four-stage Runge–Kutta scheme. Local time stepping, implicit residual smoothing, and multigrid are used to efficiently drive the solution to the steady state.

The numerical method has been successfully validated for a variety of perfect and real gas flows (see Refs. 29 and 37 and references cited therein).

In Sec. III, verification examples of the numerical code for 3D inviscid computations of perfect and dense gases and an analysis of its convergence properties are provided. For perfect gas flows, numerical results are also validated against experimental data available in the literature.

III. RESULTS

A. Preliminary verifications

For preliminary verification purposes, inviscid subsonic flows at zero angle of attack over the ONERA M-6 wing are computed. This is a swept wing with no twist that uses the symmetric ONERA D airfoil, of 10% thickness, as the wing section. The wing aspect ratio (AR) is equal to 3.8. The yaw angle is taken equal to zero for all computations presented in this study. Since the airfoil shape is symmetric and there is no incidence, then for a shock-free, inviscid flow, there should be exactly no lift and no drag as the pressure forces acting on the wing cancel.

Firstly, the flow of a perfect gas at free-stream Mach number $M_\infty=0.3$ and angle of attack $\alpha=0°$ is considered. The solution is computed by using two grids of increasing density, each composed by four zones wrapped as a C-grid about the wing leading edge. For the coarser grid, the four zones contain $24\times32\times32$, $72\times32\times32$, $72\times32\times32$, and $24\times32\times32$ cells, respectively. The finer grid has been

Downloaded 23 May 2011 to 200.17.228.160. Redistribution subject to AIP license or copyright; see http://pof.aip.org/about/rights_and_permissions

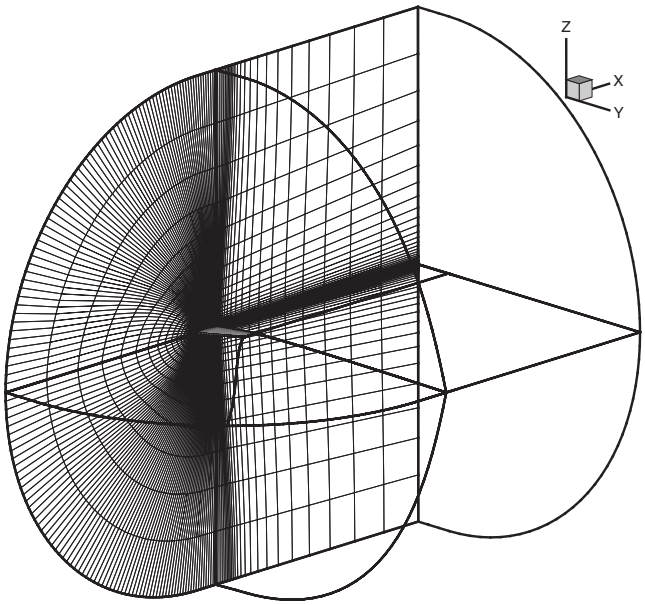

FIG. 2. View of the coarser grid used for the present study.

generated by doubling in each direction the number of cells of the coarser one. A view of the coarse grid is provided in Fig. 2.

Then, a BZT gas flow of PP10 at $M_\infty=0.8395$, $\alpha=0°$, and thermodynamic conditions $p_\infty/p_c=1.00$ and $\rho_\infty/\rho_c=0.752$, where the c subscript denotes critical quantities, is computed. For this flow, the free-stream fundamental derivative is approximately 0.416 and the flow is fully subsonic. A thorough discussion of BZT flow behavior is provided in the next section.

For both cases, the lift and drag coefficients,

$$C_L=\frac{L}{\frac{1}{2}\rho_\infty V_\infty^2 S},\quad C_D=\frac{D}{\frac{1}{2}\rho_\infty V_\infty^2 S}$$

(where L and D denote as usual the lift and drag forces, V_∞ is the free-stream velocity, and S is the wing planform area) are computed. On the present symmetric grids, the lift coefficient equals 0 within machine accuracy, whereas the drag coefficient takes small nonzero values, due to dissipation errors introduced by the numerical scheme and boundary conditions. Table I resumes results obtained for the drag coefficient in both cases and on the two grids. The computed drag coefficient decreases approximately by a factor of 5 when doubling the grid density in each direction. This roughly corresponds to a convergence order of 2.4 for the considered shock-free flow fields.

TABLE I. Computed drag coefficients for nonlifting inviscid subsonic perfect and dense gas flows at zero angle of attack past the ONERA M-6 wing.

Case	C_D
PFG flow, coarse grid	7.13×10^{-4}
PFG flow, fine grid	1.43×10^{-4}
DG flow, coarse grid	1.12×10^{-3}
DG flow, fine grid	2.15×10^{-4}

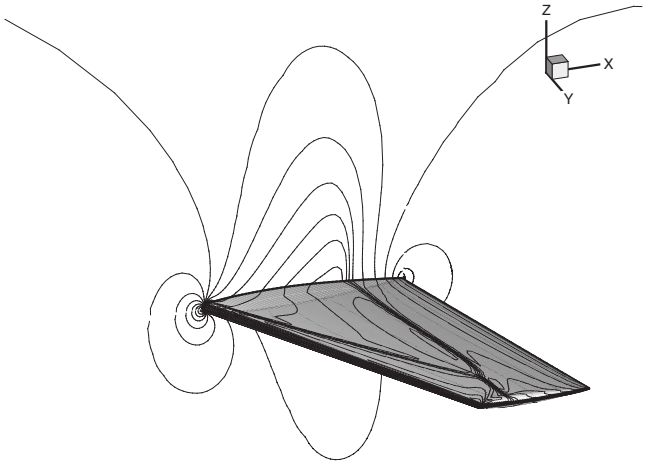

FIG. 3. Contours of the pressure coefficient for perfect gas flow over the ONERA M-6 wing. $M_\infty=0.8395$, $\alpha=3.06°$ ($\Delta C_p=0.1$).

Finally, air flow at $M_\infty=0.8395$, $\alpha=3.06°$ is computed. For this flow, experimental data by Schmidt and Charpin[40] are available for code validation; moreover, the results are taken as a reference for comparisons with dense gas flows presented in the next section. The flow field is characterized by a λ-shock located at the wing upper surface. Contours of the pressure coefficient on the coarser grid are shown in Fig. 3. In Fig. 4, the computed wall pressure coefficient distributions at three spanwise locations are compared to the experiments. Maximum differences between numerical solutions on the coarse and fine grid are within 5%. In both cases, numerical results are in reasonable agreement with experimental data. However, since the present flow model does not take into account viscous effects, shock strengths tend to be overpredicted, and the computed shock locations are downstream the experimental ones.

B. Transonic finite wing aerodynamics of dense gases

The present section provides numerical studies of transonic lifting flows of BZT gases over finite wings of different planforms and aspect ratios. Precisely, results are presented for rectangular wings by using the ONERA D airfoil as the baseline profile, characterized by three different aspect ratios, and for the ONERA M-6 swept wing. For a better understanding of the influence of 3D effects, results are compared to flows over a 2D wing at the same conditions.

All of the results presented in the following have been obtained for the following fixed values of the free-stream Mach number and angle of attack (and zero yaw):

$$M_\infty=0.8395,\quad \alpha=3.06\,°\,,$$

whereas the free-stream thermodynamic conditions (reduced pressure and density) are allowed to change. For most of the following computations the working fluid is PP10. The thermodynamic conditions considered in the present numerical experiments are represented in Fig. 5 as points of the p-v plane, referred to hereafter as the "operation points." These

Downloaded 23 May 2011 to 200.17.228.160. Redistribution subject to AIP license or copyright; see http://pof.aip.org/about/rights_and_permissions

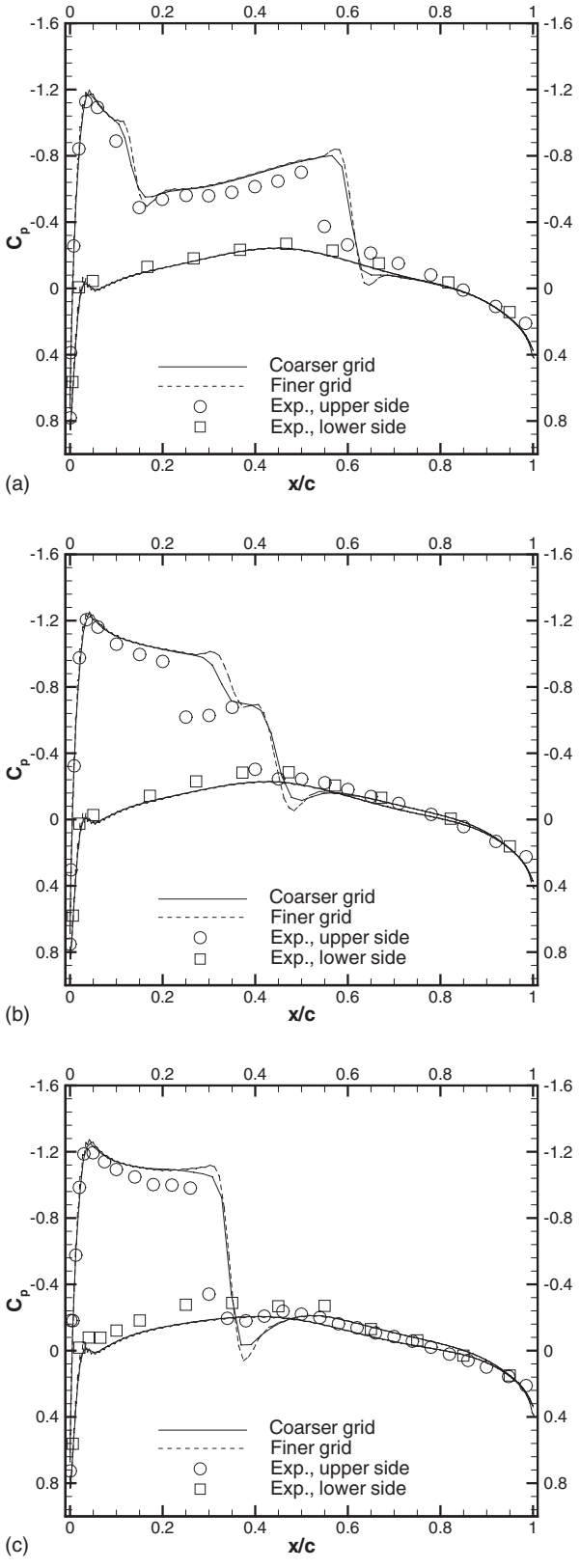

FIG. 4. Perfect gas flow over the ONERA M-6 wing, $M_\infty=0.8395$, $\alpha=3.06°$. Wall distributions of the pressure coefficient at nondimensional spanwise locations $y/b=0.44$ (a) $y/b=0.8$ (b), and $y/b=0.9$ (c). Comparison of the numerical solutions on two grids with experimental data.

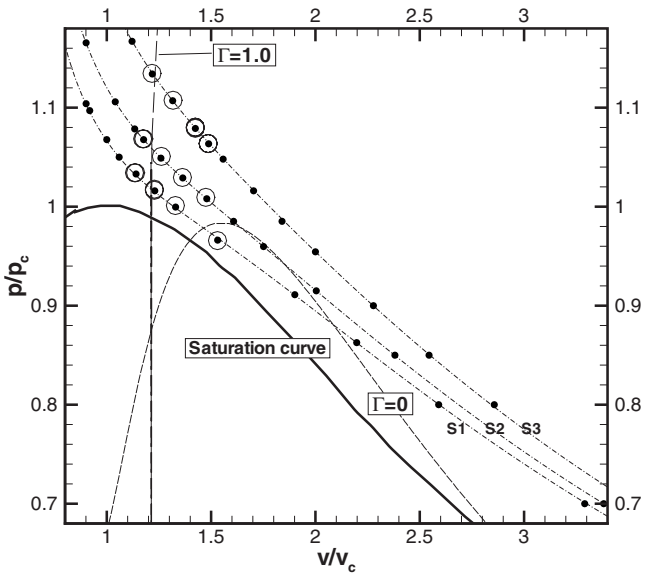

FIG. 5. Operation points (indicated by dots) used for the present parametric study. S1-3 are constant-entropy lines. For operation points marked with circles the transonic small disturbance theory [Eq. (4)] predicts subcritical flow.

points are chosen along three constant-entropy lines (denoted as S1, S2, and S3) that intersect and are (almost) tangent or external to the inversion zone, respectively. On the basis of the background knowledge of 2D BZT flows past airfoils, the flow field is expected to be subsonic for thermodynamic conditions lying closer to the inversion zone and transonic for the remaining conditions. An estimate for the critical Mach number M_c (i.e., the minimum free-stream Mach number such that the flow reaches sonic conditions at some point) has been provided by Cramer and Tarkenton[23] by using an extended transonic small disturbance (TSD) theory. Precisely, the flow is predicted to be entirely subsonic, regardless of the size of the disturbance (airfoil thickness) if

$$M_\infty < M_c = \left(1 - \frac{\Gamma_\infty^2}{\Lambda_\infty}\right)^{1/2} \approx 1 - \frac{\Gamma_\infty^2}{2\Lambda_\infty}, \tag{4}$$

where Λ_∞ is the previously defined second nonlinearity parameter,[2] representing the rate of change of Γ along an isentrope. Formula (4) is strictly valid only for flows with $M_\infty \approx 1$, $\Gamma_\infty \approx 0$, $\Lambda_\infty \approx 0$, and $\Lambda_\infty > 0$; if $\Lambda_\infty < 0$ the flow should be supercritical for all choices of $M_\infty \approx 1$. In practice, comparisons to numerical results provided in Ref. 30 show that Eq. (4) can be used to approximately predict the nature of the flow field (subcritical or supercritical) also for Γ_∞, $\Lambda_\infty = O(1)$, and $\Lambda_\infty > 0$. Operating conditions that, according to the preceding criteria, should generate subcritical flow fields are marked with circles in Fig. 5.

We now investigate dense gas flows past rectangular wings by using the ONERA D baseline airfoil. Precisely, three wings characterized by aspect ratios of 1.6, 3.6, and 7.6, respectively, are considered. Results for an infinite straight wing using the same baseline airfoil (2D case) are also reported for reference. The flow domain is discretized by means of C-grids composed of 256 cells in the direction tangent to the wall, 32 cells in the normal direction, and 40

Downloaded 23 May 2011 to 200.17.228.160. Redistribution subject to AIP license or copyright; see http://pof.aip.org/about/rights_and_permissions

TABLE II. Definition of operating conditions.

Condition	p_∞/p_c	ρ_∞/ρ_c	Γ_∞	Λ_∞
OP1	0.700	0.304	0.464	<0
OP2	1.00	0.752	0.416	>0
OP3	1.03	0.877	1.33	>0
OP4	1.05	0.944	1.62	>0

cells in the spanwise direction. The height of the first cell close to the wall is approximately 10^{-3} chords, and the outer boundary is located about 12 chords away from the wing. For the 2D case, an O-grid composed by 256×32 cells is used, with mean height of the first cell off the wall is approximately equal to 10^{-3} chords, and outer boundary located about 12 chords away from the wall.

First, typical flow patterns obtained for different operating conditions are illustrated. To this purpose, we consider in the following numerical solutions obtained for four typical choices of the operating conditions, defined in Table II and indicated as OP1-OP4. Figures 6(a)–6(d) show Mach number distributions and the $\Gamma=0$ and $\Gamma=1$ isolines for flows over the wing with AR=7.6 at the preceding conditions. In agreement with TSD theory, the flow at conditions OP1 (characterized by negative Λ_∞) is supercritical and displays a supersonic region at the upper surface that terminates with a compressive shock (located approximately at 0.45 chords at midspan), whose intensity decreases when moving from midspan to the wing tip. For flows at the same conditions over wings with lower aspect ratios, the flow is qualitatively the same, but the shock becomes weaker and closer to the leading edge; in the 2D case, the shock is located at about midchord. At conditions OP2, the free-stream fundamental derivative has almost the same value as at OP1, but Λ_∞ has opposite sign. For these conditions, the TSD theory predicts subcritical flow. This is actually verified for AR=1.6, whereas for higher aspect ratios, including the 2D case, the flow Mach number reaches values slightly higher than one. In all cases, however, the flow field is shock-free, since the fundamental derivative takes negative values over most of the wing surface (except for the immediate neighborhood of the leading and trailing edges). At conditions OP3 and OP4,

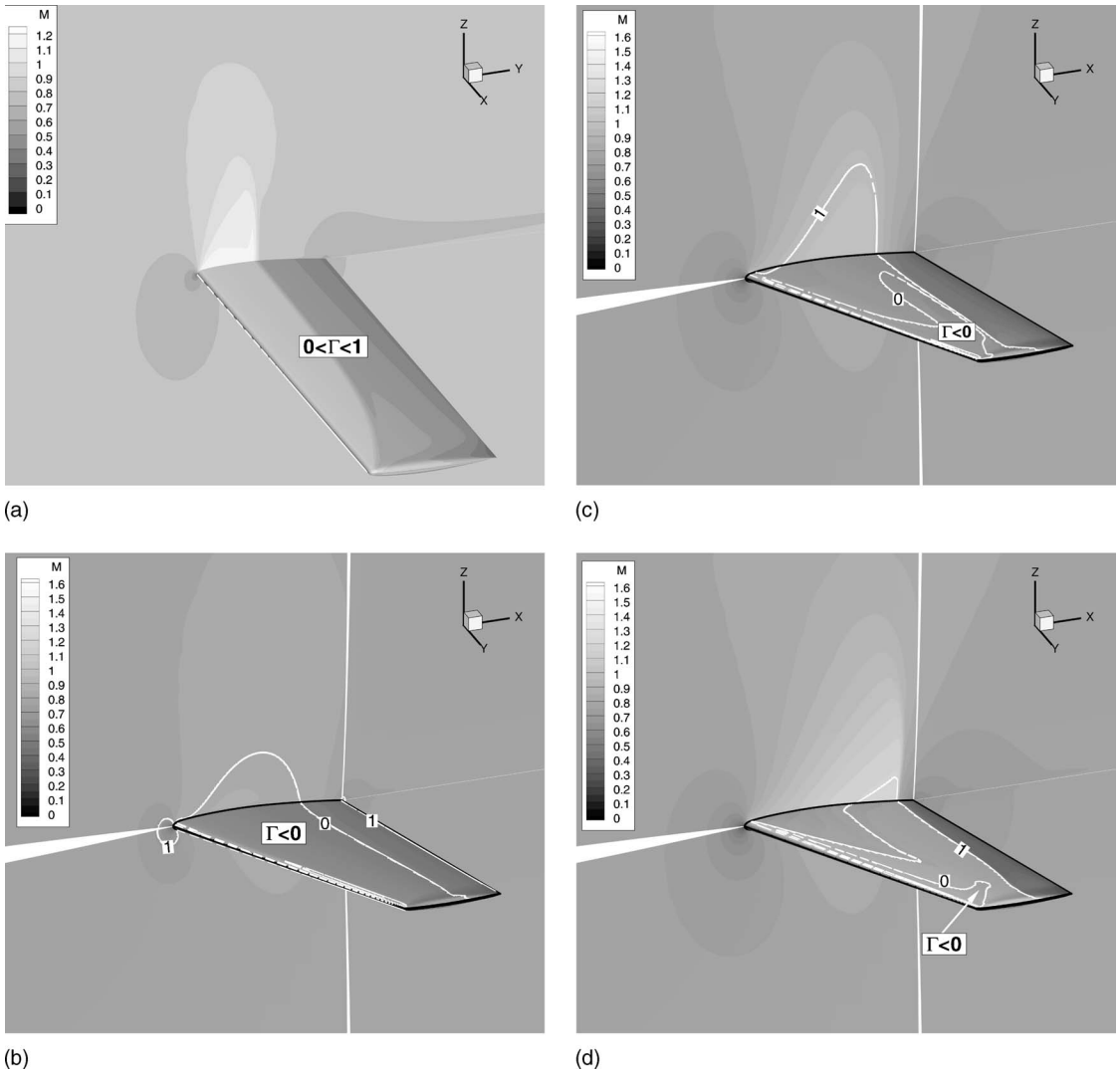

FIG. 6. Iso-Mach lines and $\Gamma=0$, $\Gamma=1$ contours for flows of PP10 over a straight wing with AR=7.6, at $M_\infty=0.8395$, $\alpha=3.06°$, and different operating conditions.

Downloaded 23 May 2011 to 200.17.228.160. Redistribution subject to AIP license or copyright; see http://pof.aip.org/about/rights_and_permissions

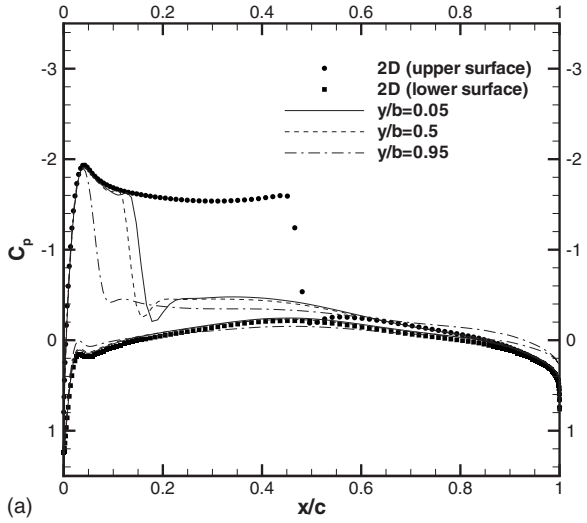

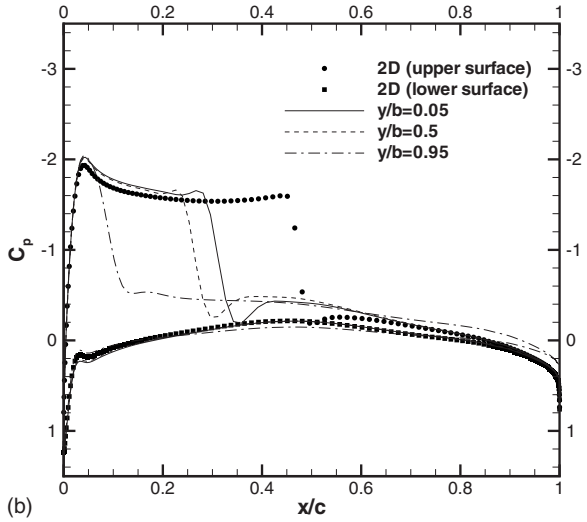

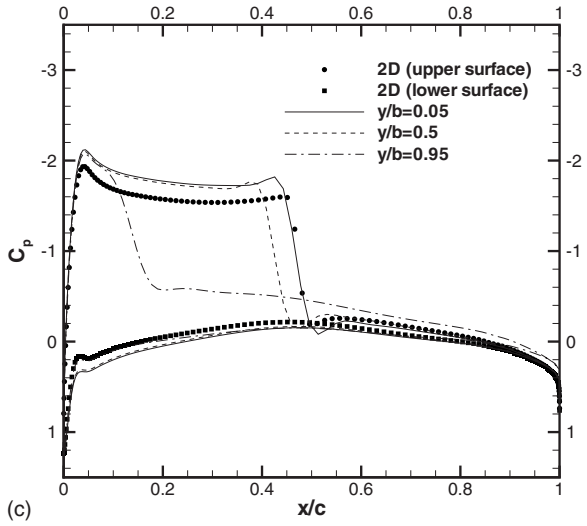

FIG. 7. Wall distributions of the pressure coefficient for flows of PP10 over rectangular wings of different aspect ratios at $M_\infty=0.8395$, $\alpha=3.06°$, and operating conditions OP1. (a) AR=1.6; (b) AR=3.6; and (c) AR=7.6.

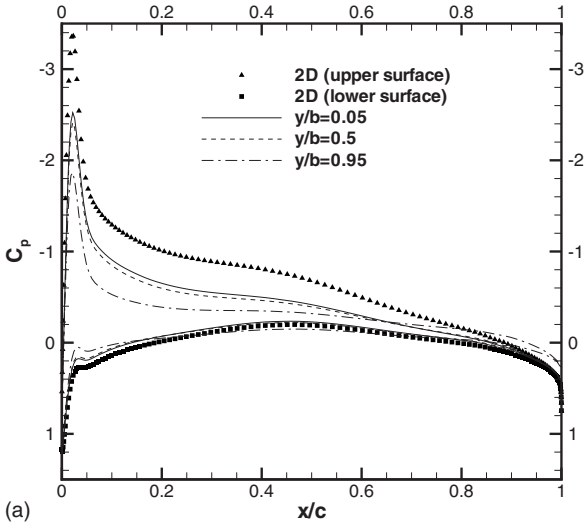

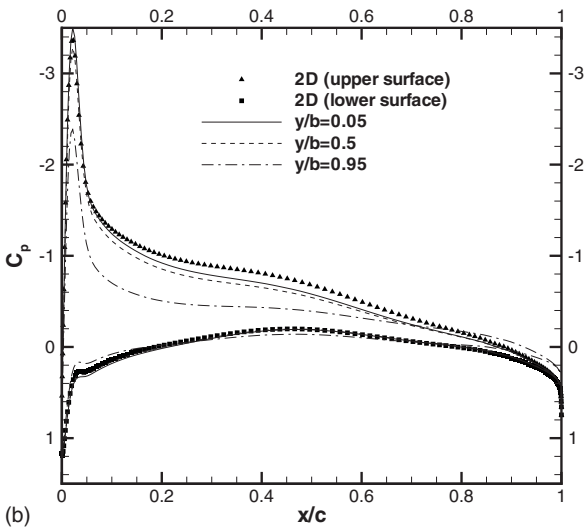

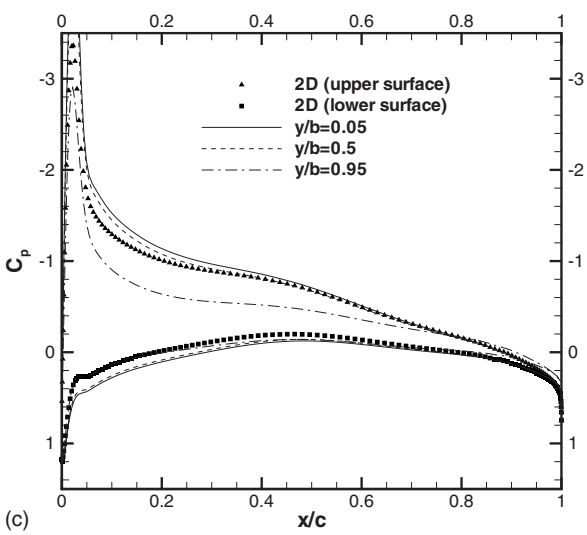

FIG. 8. Wall distributions of the pressure coefficient for flows of PP10 over rectangular wings of different aspect ratios at $M_\infty=0.8395$, $\alpha=3.06°$, and operating conditions OP2. (a) AR=1.6; (b) AR=3.6; and (c) AR=7.6.

Downloaded 23 May 2011 to 200.17.228.160. Redistribution subject to AIP license or copyright; see http://pof.aip.org/about/rights_and_permissions

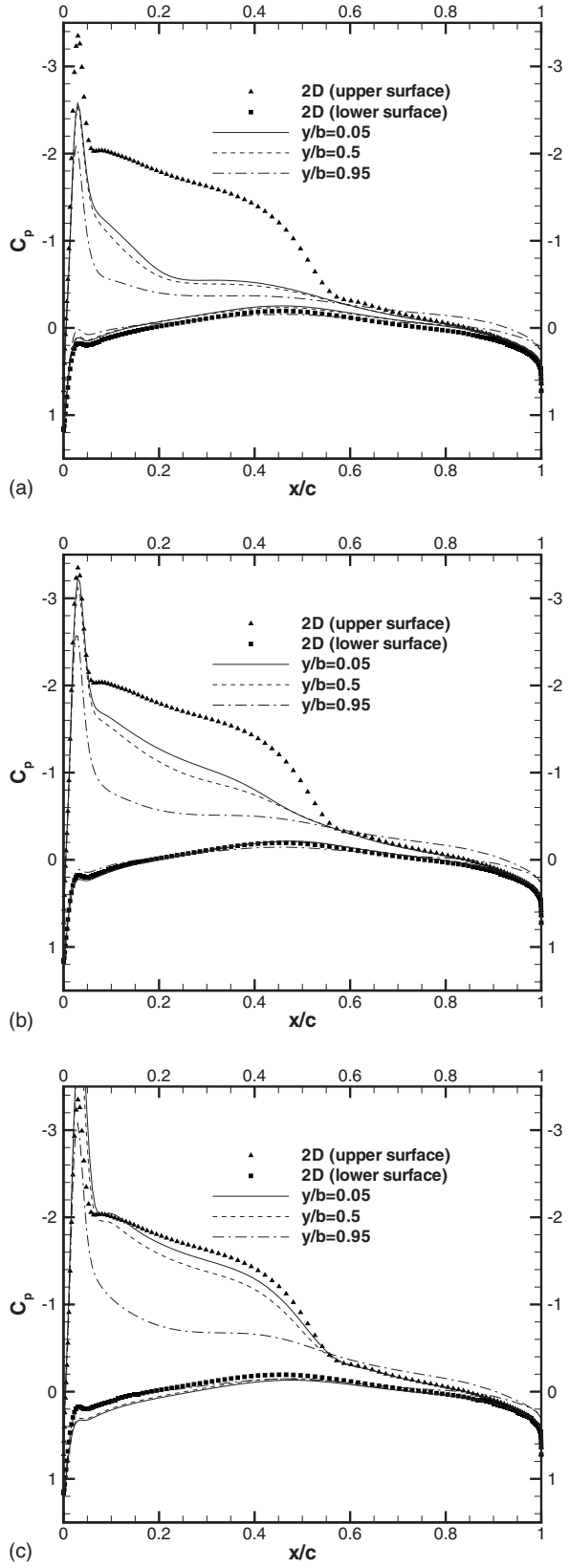

FIG. 9. Wall distributions of the pressure coefficient for flows of PP10 over rectangular wings of different aspect ratios at $M_\infty=0.8395$, $\alpha=3.06°$, and operating conditions OP3. (a) AR=1.6; (b) AR=3.6; and (c) AR=7.6.

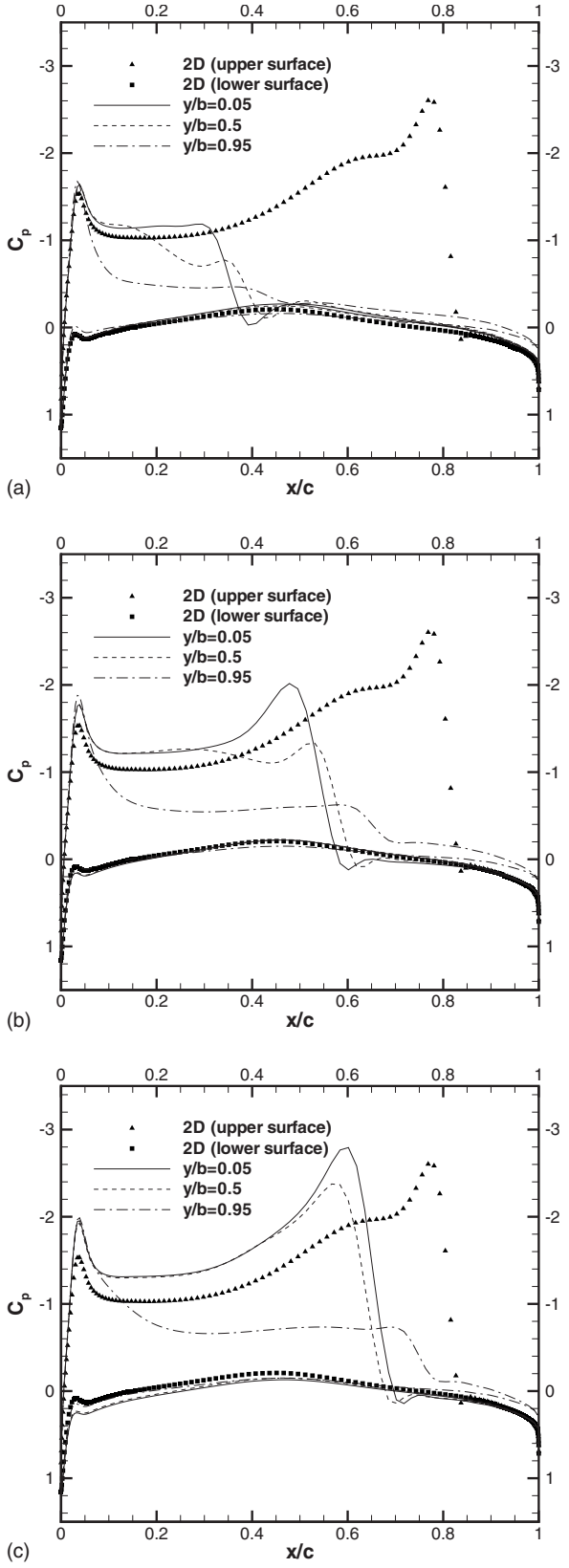

FIG. 10. Wall distributions of the pressure coefficient for flows of PP10 over rectangular wings of different aspect ratios at $M_\infty=0.8395$, $\alpha=3.06°$, and operating conditions OP4. (a) AR=1.6; (b) AR=3.6; and (c) AR=7.6

Downloaded 23 May 2011 to 200.17.228.160. Redistribution subject to AIP license or copyright; see http://pof.aip.org/about/rights_and_permissions

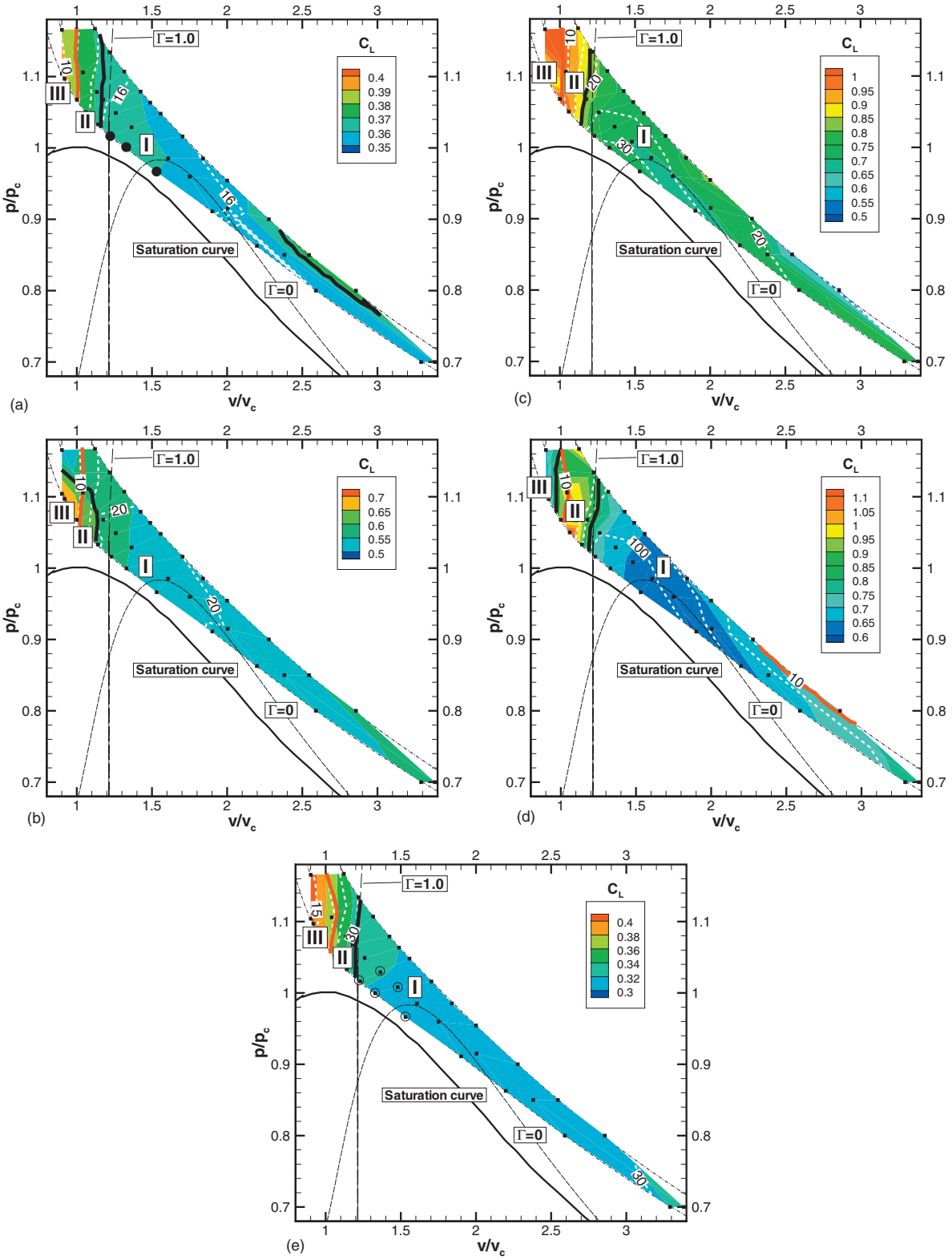

FIG. 11. (Color) Contours of the lift coefficient and isolines of the aerodynamic efficiency C_L/C_D as functions of the operating conditions in the p-v plane for different wing planforms. For points lying on the thick black lines (on the thick red lines) C_L (C_L/C_D) has the same value as in a perfect gas flow over the same configuration. (a) Straight wing, AR=1.6; (b) Straight wing, AR=3.6; (c) straight wing, AR=7.6; (d) ONERA D airfoil (AR=∞); (e) ONERA M-6 swept wing.

Downloaded 23 May 2011 to 200.17.228.160. Redistribution subject to AIP license or copyright; see http://pof.aip.org/about/rights_and_permissions

TABLE III. Mean value (denoted by $\langle\cdot\rangle$) and standard deviation (σ) of the lift coefficient C_L and aerodynamic efficiency $E=C_L/C_D$ computed for different choices of the operating conditions.

Configuration	$\langle C_L\rangle$	$\sigma(C_L)$	$\sigma(C_L)/\langle C_L\rangle\%$	$\langle E\rangle$	$\sigma(E)$	$\sigma_E/\langle E\rangle\%$	$C_{L_{\text{pfg}}}$	E_{pfg}
Straight wing, AR=1.6	0.367	1.45×10^{-2}	3.94	14.9	3.26	21.9	0.367	11.8
Straight wing, AR=3.6	0.564	5.00×10^{-2}	8.86	18.0	5.09	28.3	0.594	10.7
Straight wing, AR=7.6	0.771	1.27×10^{-1}	16.5	19.9	7.28	36.5	0.837	8.64
Straight wing, AR=∞	0.737	1.37×10^{-1}	18.7	⋯	⋯	⋯	0.829	10.3
M-6 swept wing, AR=3.8	0.333	2.79×10^{-2}	8.38	29.2	6.03	20.7	0.334	21.0

the flow field is characterized again by shock waves. At conditions OP3, however, the shock is located near the leading edge and has jump conditions close to the transition line; as a consequence, it is extremely weak. Downstream this shock, the flow enters the nonclassical region ($\Gamma<0$) where it is further compressed through a regular compression wave. At conditions OP4, the flow is characterized by a strong shock wave all along the wing span, which vanishes at wing tip. Distributions of the pressure coefficient at spanwise locations $y/b=0.05$, $y/b=0.5$, and $y/b=0.95$ (with b the halfspan) are shown in Figs. 7–10 for the preceding flow conditions and the three different values of the aspect ratio. In each plot, 2D results are also represented for reference. Note that results for all (finite) values of the aspect ratio are qualitatively similar: The main difference is the location of the shock wave, which progressively moves from the leading edge of the wing toward the midchord (2D-flow location) when the AR is increased.

Figures 11(a)–11(c) show the contour plots in the p-v plane of the computed lift coefficient and aerodynamic efficiency as functions of the operating conditions (thermodynamic conditions of the free stream) for different aspect ratios. In these plots, flood contours represent the lift coefficient distribution, and the white dashed lines connect points of equal aerodynamic efficiency. For reference, contours corresponding to lift coefficient and aerodynamic efficiency levels equal to those obtained in a perfect gas flow over the same geometry are also reported. Three main operating regions may be identified, denoted as I, II, and III in Fig. 11. In region I, characterized by $\Gamma_\infty<1$ and including points with both positive and negative Λ_∞, the aerodynamic efficiency is higher than in a perfect gas flow. This is due, as also observed in several previous papers on dense gas aerodynamics, to the disintegration of compressive shock waves and the consequent suppression of wave drag. On the other hand, in the same region the lift coefficient is somewhat lower than in a perfect gas flow. Region II is much smaller than the first one. In this region, the aerodynamic efficiency is higher than in region I because of the appearance of shock waves; nevertheless, it is considerably higher than in a perfect gas flow because of reduced losses (compared to classical flows) associated with these shocks. At the same time, the lift coefficient is higher than in a perfect gas flow. For these reasons, region II may be considered as optimal from the aerodynamic performance viewpoint. Finally, for flows at higher pressures, both the lift coefficient and the aerodynamic efficiency decrease and eventually become lower than in a perfect gas flow (within the range of operating conditions taken into account in the present study). Note that results for a 2D flows over the baseline ONERA D airfoil are qualitatively the same, except for much higher values of the aerodynamic efficiency (especially in region I), due to the absence of the induced drag.

The results of Fig. 11 show that the borderlines between the different regimes are not very sensitive to the aspect ratio (and to the wing planform, as discussed later). Conversely, the aerodynamic performance (lift coefficient and efficiency) dramatically decreases with AR. On the other hand, for low values of the aspect ratio, the aerodynamic coefficients are less sensitive to the operating conditions. Table III reports the mean value, the standard deviation, and the coefficient of variation (ratio of the standard variation to the mean) of the aerodynamic coefficients computed for different operating conditions. Results show that dense gas flows perform better, in average, compared to perfect gas flows over the same configuration. The best mean performance (higher C_L and C_L/C_D) over the considered range of operating conditions is provided by the configuration characterized by the highest aspect ratio, which is coherent with classical aerodynamic theory. On the other hand, high-aspect-ratio configurations are also more sensitive to the operating conditions, as confirmed by the high computed values of the standard deviation for both the lift coefficient and aerodynamic efficiency. In particular, for a wing with AR=7.6, the aerodynamic efficiency dramatically drops below the perfect gas value as the pressure increases. Conversely, for a wing with AR=1.6, the aerodynamic performance remains higher, or at least similar, to that of a perfect gas over the whole range of conditions.

In order to verify how well analytic models used in transonic wing design for flows of perfect gases apply to dense gas flows, separate contributions of the wave drag and of the induced drag coefficients and their sum (i.e., the total drag coefficient) are computed by using some current-use relations for transonic aerodynamics. On the one hand, the wave drag generated by the baseline airfoil is estimated by using the so-called Korn formula,[41] which relates the drag divergence Mach number M_{dd} (empirically defined as the point on the drag polar $c_d=c_d(M_\infty)$ $-c_d$ being the profile drag coefficient-where $\partial c_d/\partial M_\infty=0.1$) to the baseline section lift coefficient c_l, and to some geometrical parameters, such as the relative section thickness t/c and the sweep angle Φ,

Downloaded 23 May 2011 to 200.17.228.160. Redistribution subject to AIP license or copyright; see http://pof.aip.org/about/rights_and_permissions

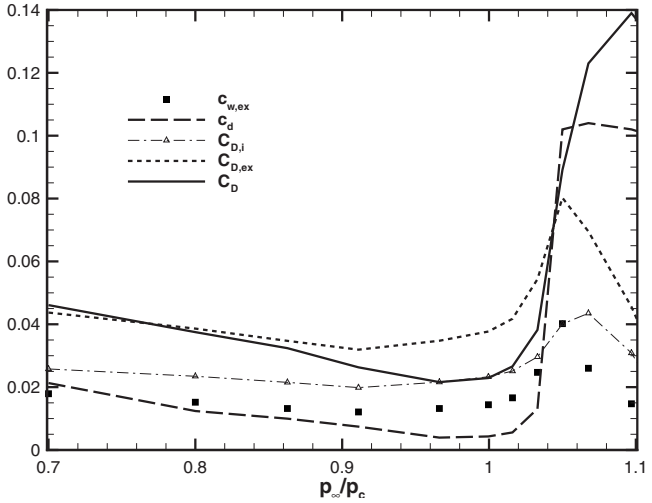

FIG. 12. Variation of the drag coefficient with operating conditions for a rectangular wing with AR=7.6. The computed numerical results for C_D are compared to results for 2D flow over the same baseline airfoil (c_d) and to results predicted by means of analytic relationships of common use in perfect gas flow transonic aerodynamics ($C_{D,\mathrm{ex}}$). These are obtained by applying the Korn formula (Ref. 41) for computing the wave drag ($c_{w,\mathrm{ex}}$) and the classical lifting-line theory for the induced drag $C_{D,i}$.

$$M_{dd} = \frac{\kappa_A}{\cos\Phi} - \frac{(t/c)}{\cos^2\Phi} - \frac{c_l}{10\cos^3\Phi}, \tag{5}$$

with κ_A a "technological factor," equal to 0.87 for airfoils of the NACA six-digit series and to 0.95 for supercritical airfoils. In addition to the Korn formula, an empirical relation is often used to describe the transonic drag rise,[42]

$$c_d = 20(M_\infty - M_c, 0)^4, \quad (M_\infty > M_c). \tag{6}$$

The preceding relation may be derived, providing an equation relating the drag divergence Mach number and the critical Mach number M_c (see Ref. 41),

$$M_c = M_{dd} - (0.1/80)^{1/3}.$$

This can be injected into Eq. (6), finally yielding the wing section wave drag expected for the considered lift level. On the other hand, induced drag may been computed through the well-known formula (see, e.g., Ref. 43),

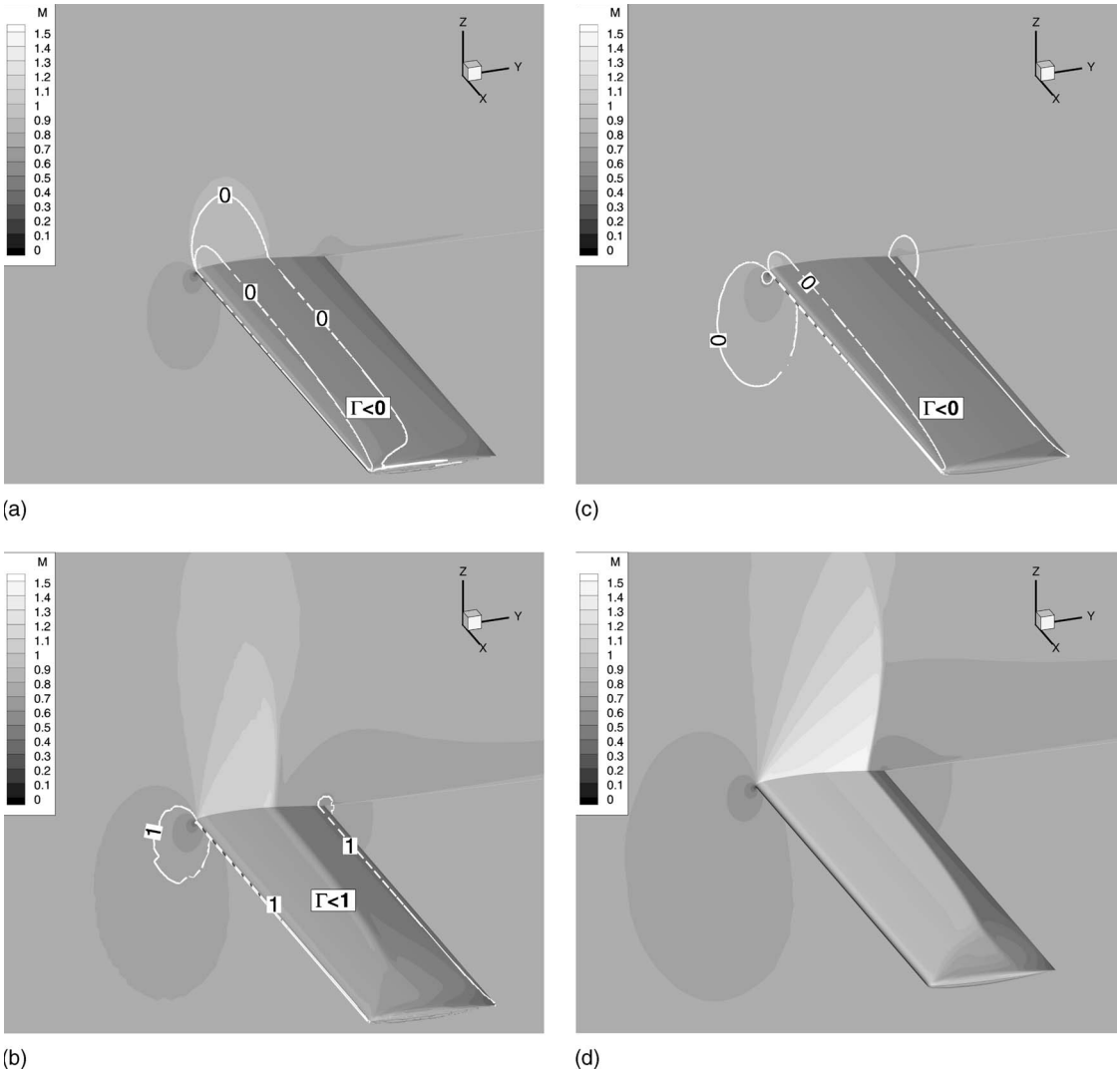

FIG. 13. Iso-Mach lines for flows over a rectangular wing with AR=7.6, at M_∞=0.8395, α=3.06°, p_∞/p_c=0.967, ρ_∞/ρ_c=0.653, and three organic working fluids. (a) siloxane D5, (b) toluene, and (c) fluorocarbon PP10.

Downloaded 23 May 2011 to 200.17.228.160. Redistribution subject to AIP license or copyright; see http://pof.aip.org/about/rights_and_permissions

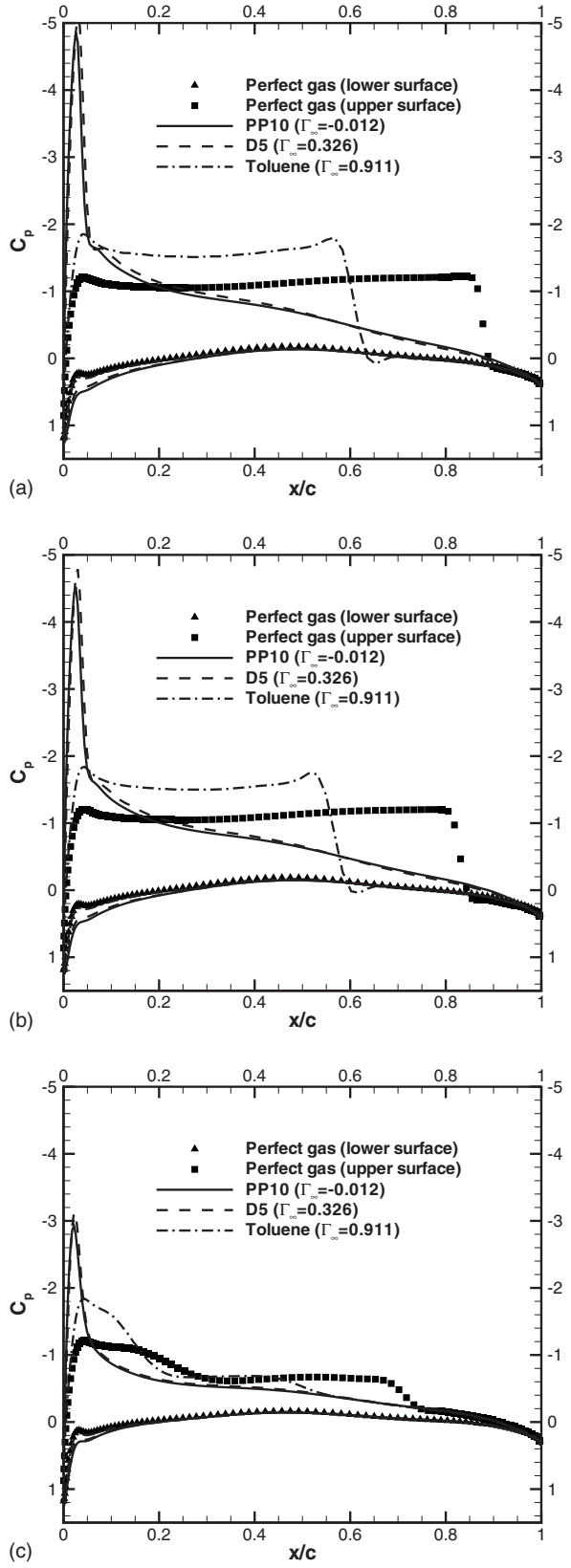

FIG. 14. Wall pressure coefficient distributions for flows of different working fluids over a rectangular wing with AR=7.6, at $M_\infty=0.8395$, $\alpha=3.06°$, $p_\infty/p_c=0.967$, $\rho_\infty/\rho_c=0.653$. (a) $y/b=0.05$, (b) $y/b=0.5$, and (c) $y/b=0.95$.

$$C_{D,i}=\frac{C_L^2}{e\pi \mathrm{AR}}, \tag{7}$$

where the wing efficiency factor e has been assumed equal to 0.97. Note that, strictly speaking, relation (7) is valid only for incompressible flows over high-aspect-ratio wings. The expected total drag $C_D=c_d+C_{D,i}$ for the wing with AR=7.6 is plotted in Fig. 12 for several operating conditions selected along isentrope S1 and compared to the numerical results. The empirical relations described above overestimate the computed drag coefficient over a wide range of conditions. This is essentially due to the fact that relation (5) applied to dense gas flows overestimates the wave drag produced for a given lift level in the region of conditions where dense gas effects are stronger. For flows operating at high pressures, the trend is reversed: Here, the strong compressibility effects characterizing high-Γ_∞ flows lead to the formation of much stronger shock waves (and much higher wave drag) than predicted by the perfect gas theory.

To verify how sensitive the computed results are to the working fluid, numerical simulations have been performed for the AR=7.6 wing by using the MAH model with coefficients corresponding to the BZT siloxane D5 and to toluene. Figures 13 and 14 compare the solutions obtained at operating conditions $p_\infty/p_c=0.967$, $\rho_\infty/\rho_c=0.653$ for these working fluids (for which Γ_∞ is equal to 0.326 and 0.911, respectively, and $\Lambda_\infty>0$) and for PP10 ($\Gamma_\infty=-0.121$, $\Lambda_\infty>0$). The perfect gas solution is also reported for reference. Precisely, Fig. 13 displays the iso-Mach contours and the $\Gamma=0$ and $\Gamma=1$ isolines, and Fig. 14 shows the wall distributions of the pressure coefficient at three spanwise locations. Results for the two BZT fluids, D5, and PP10 are qualitatively similar: In both cases, the resulting flow field is almost shock-free and characterized by values of the fundamental derivative below 1 over most of the wing surface. Instead, toluene results are characterized by a strong shock located at the wing upper surface and are, at least qualitatively, closer to those obtained for a perfect gas. A parametric study for different values of the free-stream pressure has also been performed. Figure 15 displays plots of the fundamental derivative, the maximum value of Mach number, the lift coefficient, and the aerodynamic efficiency versus the reduced free-stream pressure for the three substances under investigation. Results obtained for D5 and PP10 are qualitatively and quantitatively close to each other over the whole range of conditions considered for the study. Results for toluene are also relatively close to those of the BZT fluids whenever the free-stream values of Γ for the three fluids are similar. Conversely, toluene curves for the aerodynamic coefficients exhibit a clear departure from those for the BZT fluids for $p_\infty/p_c \gtrapprox 0.83$. In this region $\Gamma \approx O(1)$ for toluene, whereas $|\Gamma| \ll 1$ for the BZT fluids. As a consequence, shock waves in toluene are stronger than in BZT flows at approximately the same reduced conditions, even if the upstream Mach number is almost the same.

The last series of results concerns BZT flows over the ONERA M-6 swept wing (AR=3.8). Flow patterns obtained at operating conditions OP1–OP4 are represented in Fig. 16. Typical wall distributions of the Mach number and pressure coefficient at two spanwise locations are shown in Fig. 17.

Downloaded 23 May 2011 to 200.17.228.160. Redistribution subject to AIP license or copyright; see http://pof.aip.org/about/rights_and_permissions

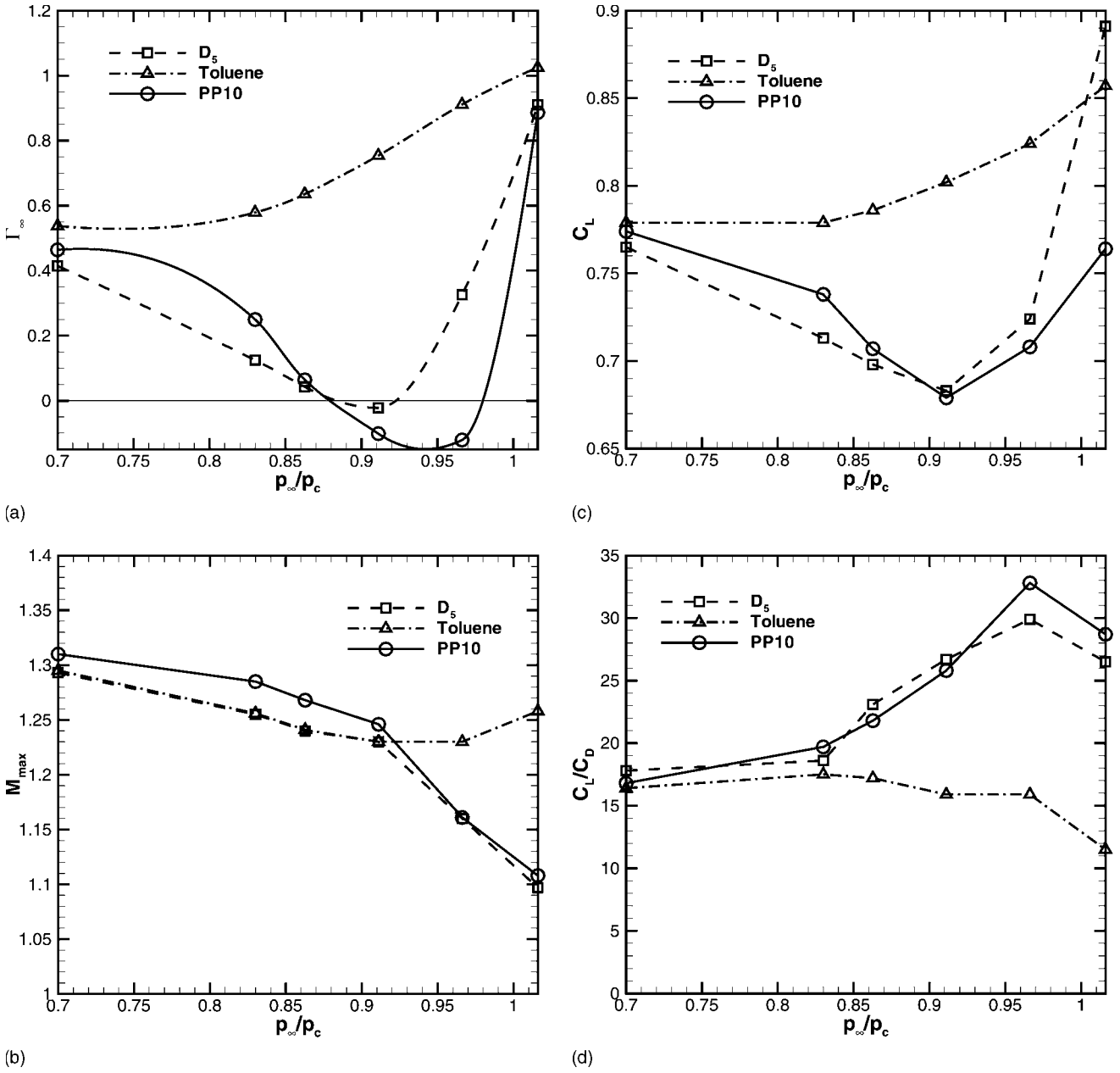

FIG. 15. Flows of organic working fluids over a rectangular wing with AR=7.6, at M_∞=0.8395, α=3.06° and different operating pressures: (a) free-stream fundamental derivative, (b) maximum value of the Mach number in the flow field, (c) lift coefficient, and (d) aerodynamic efficiency.

Both for conditions OP1 and OP2, the flow is fully subsonic. However, comparisons to results obtained for a straight wing with approximately the same aspect ratio suggest that, at conditions OP1 (which lie outside the inversion zone), the appearance of shock waves is delayed mainly by effect of the sweep angle; conversely, at conditions OP2, it results from the combined effect of BZT effects and of the sweep angle. At conditions OP3 and OP4, the free-stream Mach number is always above the critical value predicted by Eq. (4) and actually the computed flow fields are supercritical. However, at conditions S3, the maximum Mach number in the flow is just slightly above 1, and the flow evolves almost isentropically, whereas at conditions S4 BZT effects begin to fade, and a compression shock forms at the rear part of the upper surface. However, losses associated with this shock are still relatively weak, the upstream Mach number being close to 1, and the fundamental derivative close to zero.

The computed aerodynamic performance for different choices of the operating conditions is represented in Fig. 11(e). Contours of the aerodynamic performance for the swept wing are qualitatively close to those obtained for straight wings, and again three main regimes may be identified. Looking more closely at the computed performance (Table III), the average lift coefficient computed over the considered range of conditions is almost equal to that computed for a perfect gas flow over the same configuration, whereas the average efficiency is about 30% higher, mostly due to wave drag reduction. On the other hand, the lift coefficient is lower compared to that obtained for a rectangular wing with a similar aspect ratio, as predicted by classical

Downloaded 23 May 2011 to 200.17.228.160. Redistribution subject to AIP license or copyright; see http://pof.aip.org/about/rights_and_permissions

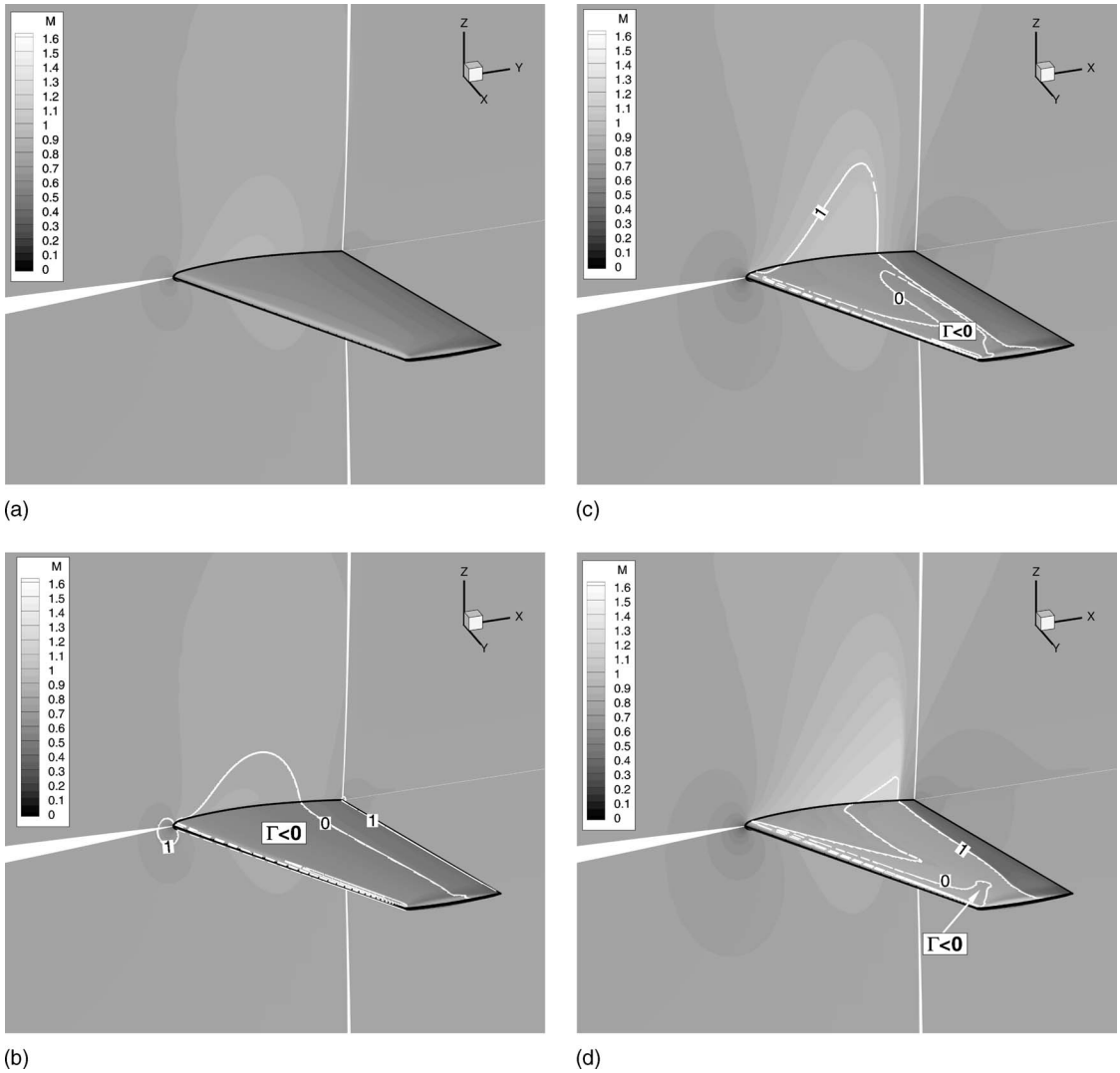

FIG. 16. Iso-Mach lines for flows over the ONERA M-6 wing, $M_\infty=0.8395$, $\alpha=3.06°$, and different operating conditions.

swept wing theory. Note that in the dense gas flow nonclassical effects contribute, already for a straight wing, to reduce wave drag; as a consequence, advantages deriving from the use of a swept wing become less significant. However, for the swept wing, the relative standard deviation of the aerodynamic efficiency is lower compared to the straight wing: In fact, the use of a nonzero sweep angle allows conserving low values of the wave drag even at operating conditions where dense gas effects are less significant. Clearly, the sweep angle adopted for the M-6 wing is not optimal for dense gas flows and should be optimized: It is likely that a small value of the sweep angle is already sufficient to ensure a good trade-off between peak performance and stability to variations of the operating conditions.

IV. CONCLUSIONS

In this paper, a detailed numerical study of 3D flows of dense gases of the BZT type over finite wings has been presented. Present results show that the main flow regimes identified in previous 2D studies are also found in 3D flows, regardless to the particular wing planform or aspect ratio.

Namely, for free-stream thermodynamic conditions such that the fundamental derivative in the freestream is close to zero, the flow critical Mach number dramatically increases with respect to a perfect gas flow over the same configuration, the flow field remains shock-free, and no wave drag appears. Of course, in 3D flow, the appearance of induced drag leads to finite, albeit high values of the aerodynamic efficiency. Just like in 2D flows, the lift coefficient is lower than the reference perfect gas value in this regime. For higher values of the operating pressure (and fundamental derivative), the flow becomes supercritical and shocks appear. This considerably improves the lift coefficient, but a wave drag component is now present. However, since shocks have jump conditions in the vicinity of the transition line, the associated losses are much lower than usual and the corresponding generated wave drag is very small. This leads to higher aerodynamic efficiency than in a perfect gas flow. Once again, due to induced drag (that grows as the square of the lift coefficient), the observed improvements over a perfect gas remain within about 50%, whereas for a 2D BZT flow, the aerodynamic efficiency can be up to one order of

Downloaded 23 May 2011 to 200.17.228.160. Redistribution subject to AIP license or copyright; see http://pof.aip.org/about/rights_and_permissions

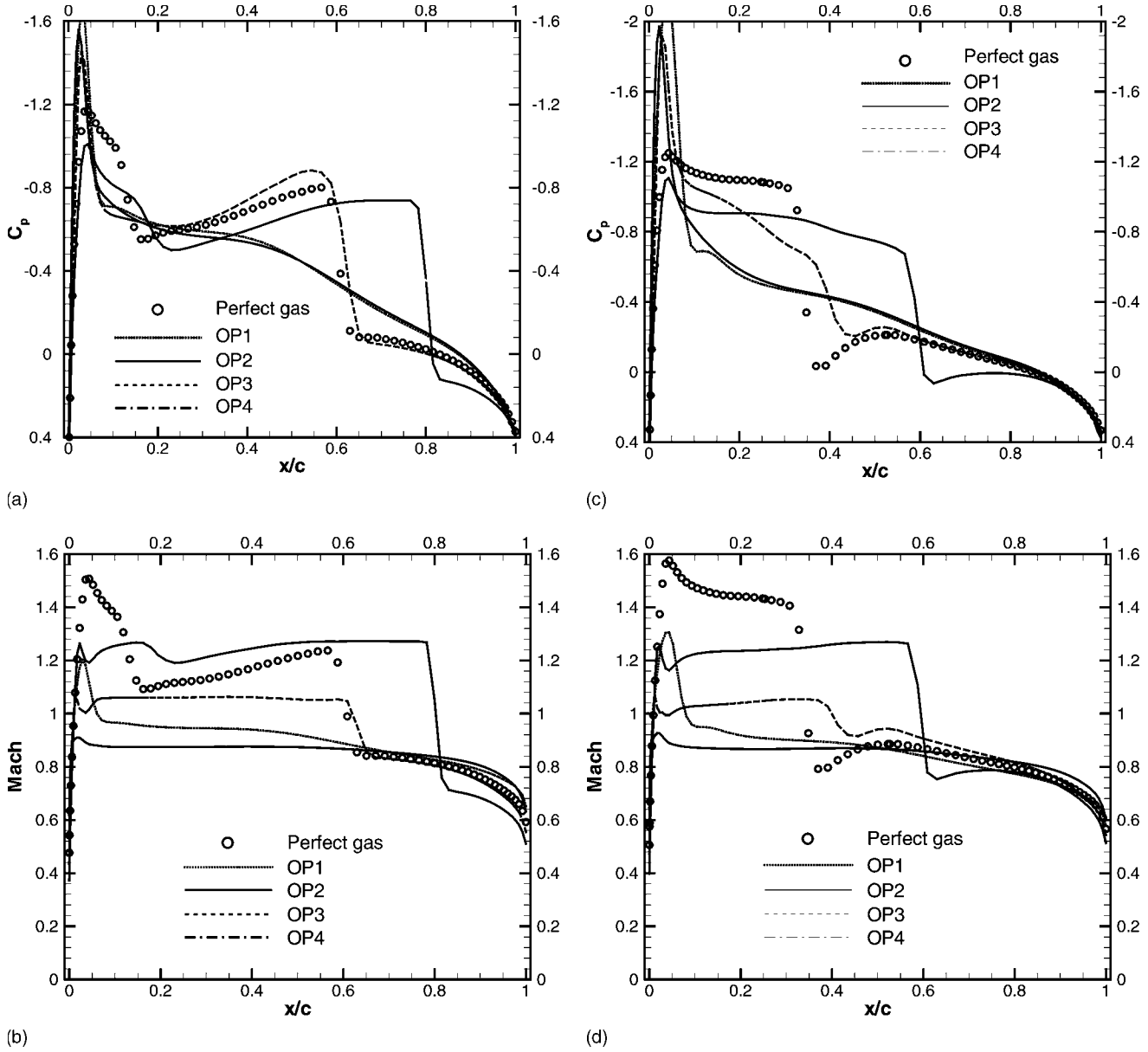

FIG. 17. Distributions of the pressure coefficient and Mach number on the wing upper surface, at nondimensional spanwise locations $y/b=0.44$ [(a) and (b)] and $y/b=0.9$ [(c) and (d)]. Comparison of the numerical solutions for perfect gas flow and for BZT flows at different operating conditions.

magnitude greater than in a 2D perfect gas flow at the same conditions. Finally, for higher values of the free-stream pressure/fundamental derivative, the flow is characterized by strong shocks and the advantages of using a BZT working fluid disappear.

The main effect of the wing aspect ratio is, on the one hand, to affect the aerodynamic performance: Namely, for higher values of the aspect ratio both the lift coefficient and the aerodynamic performance increase, as in classical perfect gas flows. On the other hand, for higher aspect ratios, the results are more sensitive to the operating conditions, and the aerodynamic performance decays more quickly when the operation point moves away from the dense gas region.

The effect of the sweep angle has been also investigated. As in classical transonic wing theory, the use of a sweep angle delays the first appearance of supercritical flow and the transonic drag rise. On the other hand, it reduces the lift coefficient. For dense gas flows, the use of a sweep angle leads to lower efficiency gains than in perfect gas flows, since the drag rise is already delayed by dense gas effects over a large range of operating conditions. However, for dense gas flows over a swept wing, the aerodynamic performance is less sensitive to the operating conditions than for flows over a straight wing with the same aspect ratio, since the sweep angle allows conserving high values of the aerodynamic efficiency even for flow conditions where dense gas effects begin to disappear. Most likely the use of a smaller sweep angle may represent a good trade-off solution, to be investigated in future work.

As a final remark, the present study has been restricted to inviscid flows. When viscous effects are taken into account (see Ref. 30), further gains are to be expected from the reduction of losses due to shock/boundary layer interaction and separation, which can made the use of BZT working

Downloaded 23 May 2011 to 200.17.228.160. Redistribution subject to AIP license or copyright; see http://pof.aip.org/about/rights_and_permissions

fluids for practical applications actually worthy to be considered.

[1] P. A. Thompson, "A fundamental derivative in gas dynamics," Phys. Fluids **14**, 1843 (1971).
[2] M. S. Cramer and A. Kluwick, "On the propagation of waves exhibiting both positive and negative nonlinearity," J. Fluid Mech. **142**, 9 (1984).
[3] G. D. LeFloch, *Hyperbolics Systems of Conservation Laws: The Theory of Classical and Nonclassical Shock Waves* (Birkhauser, Basel, 2002).
[4] P. A. Thompson, and K. C. Lambrakis, "Negative shock waves," J. Fluid Mech. **60**, 187 (1973).
[5] M. S. Cramer, "Negative nonlinearity in selected fluorocarbons," Phys. Fluids A **1**, 1894 (1989).
[6] A. Guardone and B. M. Argrow, "Nonclassical gasdynamic region of selected fluorocarbons," Phys. Fluids **17**, 116102 (2005).
[7] P. Colonna and P. Silva, "Dense gas thermodynamic properties of single and multi-component fluids for fluid dynamic simulations," ASME J. Fluids Eng. **125**, 414 (2003).
[8] P. Colonna and A. Guardone, "Molecular interpretation of nonclassical gas dynamics of dense vapors under the van der Waals model," Phys. Fluids **18**, 056101 (2006).
[9] P. A. Thompson, "Liquid-vapor adiabatic phase changes and related phenomena," in *Nonlinear Waves in Real Fluids*, edited by A. Kluwick (Springer-Verlag, New York, 1991), pp. 147–213.
[10] P. A. Thompson and Y. Kim, "Direct observation of shock splitting in a vapor-liquid system," Phys. Fluids **26**, 3211 (1983).
[11] P. A. Thompson, G. A. Carofano, and Y. Kim, "Shock waves and phase changes in a large heat capacity fluid emerging from a tube," J. Fluid Mech. **166**, 57 (1986).
[12] A. A. Borisov, Al. A. Borisov, S. S. Kutateladze, and V. E. Nakaryakov, "Rarefaction shock waves near the critic liquid-vapour point," J. Fluid Mech. **126**, 59 (1983).
[13] S. S. Kutateladze, V. E. Nakaryakov, and A. A. Borisov, "Rarefaction waves in liquid and gas-liquid media," Annu. Rev. Fluid Mech. **19**, 577 (1987).
[14] M. S. Cramer and R. Sen, "Shock formation in fluids having embedded regions of negative nonlinearity," Phys. Fluids **29**, 2181 (1986).
[15] S. H. Fergason, T. H. Ho, B. M. Argrow, and G. Emanuel, "Theory for producing a single-phase rarefaction shock-wave in a shock tube," J. Fluid Mech. **445**, 37 (2001).
[16] C. Zamfirescu, A. Guardone, and P. Colonna, "Numerical simulation of the FAST dense gas experiment," in Proceedings of the ECCOMAS CFD 2006, TU Delft, the Netherlands, 2006, edited by P. Wesseling, E. Oñate, and J. Périaux (TU Delft, Delft, The Netherlands, 2006).
[17] R. Menikoff and B. J. Plohr, "The Riemann problem for fluid flow of real materials," Rev. Mod. Phys. **61**, 75 (1989).
[18] M. S. Cramer, "Nonclassical dynamics of classical gases," in *Nonlinear Waves in Real Fluids*, edited by A. Kluwick (Springer-Verlag, New York, 1991), pp. 91–145.
[19] A. Kluwick, *Handbook of Shockwaves* (Academic, New York, 2000), Vol. 1, Chap. 3.4, pp. 339–411.
[20] M. S. Cramer and L. M. Best, "Steady, isentropic flows of dense gases," Phys. Fluids A **3**, 219 (1991).
[21] B. M. Argrow, "Computational analysis of dense shock tube flow," Shock Waves **6**, 241 (1996).
[22] B. P. Brown and B. M. Argrow, "Nonclassical dense gas flows for simple geometries," AIAA J. **36**, 1842 (1998).
[23] M. S. Cramer and G. M. Tarkenton, "Transonic flows of Bethe–Zel'dovich–Thompson fluids," J. Fluid Mech. **240**, 197 (1992).
[24] S. H. Morren, "Transonic aerodynamics of dense gases," Masters thesis, Engineering Science and Mechanics Department, Virginia Polytecnic Institue and State University, 1991 (also published as NASA Report No. TM 103732, 1991).
[25] Z. Rusak and C. W. Wang, "Transonic flow of dense gases around an airfoil with a parabolic nose," J. Fluid Mech. **346**, 1 (1997).
[26] C. W. Wang and Z. Rusak, "Numerical studies of transonic BZT gas flows around thin airfoils," J. Fluid Mech. **396**, 109 (1999).
[27] J. F. Monaco, M. S. Cramer, and L. T. Watson, "Supersonic flows of dense gases in cascade configurations," J. Fluid Mech. **330**, 31 (1997).
[28] B. P. Brown and B. M. Argrow, "Application of Bethe–Zel'dovich–Thompson in organic Rankine cycles," J. Propul. Power **16**, 1118 (2000).
[29] P. Cinnella and P. M. Congedo, "Aerodynamic performance of transonic Bethe–Zel'dovich–Thompson flows past an airfoil," AIAA J. **43**, 370 (2005).
[30] P. Cinnella and P. M. Congedo, "Inviscid and viscous aerodynamics of dense gases," J. Fluid Mech. **580**, 179 (2007).
[31] J. J. Martin and Y. C. Hou, "Development of an equation of state for gases," AIChE J. **1**, 142 (1955).
[32] B. Lakshminarayama, *Fluid Dynamics and Heat Transfer of Turbomachinery* (Wiley, New York, 1996).
[33] S. Fergason, A. Guardone, and B. M. Argrow, "Construction and validation of a dense gas shock tube," J. Thermophys. Heat Transfer **17**, 326 (2003).
[34] A. Guardone, "Three-dimensional shock-tube flows for dense gases," J. Fluid Mech. **583**, 423 (2007).
[35] G. Emanuel, "Assessment of the Martin–Hou equation for modelling a nonclassical fluid," J. Fluids Eng. **116**, 883 (1994).
[36] A. Guardone, L. Vigevano, and B. M. Argrow, "Assessment of thermodynamic models for dense gas dynamics," Phys. Fluids **16**, 3878 (2004).
[37] P. Cinnella and P. M. Congedo, "Numerical solver for dense gas flows," AIAA J. **43**, 2458 (2005).
[38] A. Jameson, W. Schmidt, and E. Turkel, "Numerical solutions of the Euler equations by finite volume methods using Runge–Kutta time stepping," AIAA Report No. 81–1259, 1981.
[39] A. Rezgui, P. Cinnella, and A. Lerat, "Third-order-accurate finite volume schemes for Euler computations on curvilinear meshes," Comput. Fluids **30**, 875 (2001).
[40] V. Schmitt and F. Charpin, "Pressure distributions on the ONERA-M6 wing at transonic Mach numbers," Fluid Dynamics Panel Working Group 04, Report No. AGARD AR 138, 1979.
[41] W. H. Mason, "Analytic models for technology integration in aircraft design," AIAA Paper No. 90–3262, 1990.
[42] W. F. Hilton, *High Speed Aerodynamics* (Longmans, London, 1952), pp. 47–49.
[43] J. D. Anderson, *Fundamentals of Aerodynamics*, 4th ed. (McGraw-Hill, New York, 2005), Chap. 5.

Downloaded 23 May 2011 to 200.17.228.160. Redistribution subject to AIP license or copyright; see http://pof.aip.org/about/rights_and_permissions